OPEN ACCESS



The Dust Sublimation Region of the Type 1 AGN NGC 4151 at a Hundred Microarcsecond Scale as Resolved by the CHARA Array Interferometer

Makoto Kishimoto ¹, Matthew Anderson², Theo ten Brummelaar², Christopher Farrington², Robert Antonucci³, Sebastian Hönig ⁴, Florentin Millour⁵, Konrad R. W. Tristram ⁶, Gerd Weigelt ⁷, Laszlo Sturmann², Judit Sturmann², Gail Schaefer ², and Nic Scott²

Department of Astrophysics & Atmospheric Sciences, Kyoto Sangyo University, Kamigamo-motoyama, Kita-ku, Kyoto 603-8555, Japan; mak@cc.kyoto-su.ac.jp Georgia State University Center for High Angular Resolution Astronomy Array, Mount Wilson Observatory, USA

Department of Physics, University of California, Santa Barbara, USA

Department of Physics & Astronomy, University of Southampton, UK

⁵ Laboratoire Lagrange, Université Côte d'Azur, Observatoire de la Côte d'Azur, CNRS, Nice, France European Southern Observatory, Alonso de Córdova 3107, Vitacura, Santiago, Chile ⁷ Max Planck Institute for Radio Astronomy, Bonn, Germany

Received 2022 May 17; revised 2022 August 30; accepted 2022 September 12; published 2022 November 17

Abstract

The nuclear region of Type 1 active galactic nuclei (AGNs) has only been partially resolved so far in the near-infrared (IR), where we expect to see the dust sublimation region and the nucleus directly without obscuration. Here, we present the near-IR interferometric observation of the brightest Type 1 AGN NGC 4151 at long baselines of \sim 250 m using the CHARA Array, reaching structures at hundred microarcsecond scales. The squared visibilities decrease down to as low as \sim 0.25, definitely showing that the structure is resolved. Furthermore, combining with the previous visibility measurements at shorter baselines but at different position angles, we show that the structure is elongated *perpendicular* to the polar axis of the nucleus, as defined by optical polarization and a linear radio jet. A thin-ring fit gives a minor/major axis ratio of \sim 0.7 at a radius \sim 0.5 mas (\sim 0.03 pc). This is consistent with the case where the sublimating dust grains are distributed preferentially in the equatorial plane in a ring-like geometry, viewed at an inclination angle of \sim 40°. The recent mid-IR interferometric finding of polar-elongated geometry at a pc scale, together with a larger-scale polar outflow as spectrally resolved by the Hubble Space Telescope, would generally suggest a dusty, conical and hollow outflow being launched, presumably in the dust sublimation region. This might potentially lead to a polar-elongated morphology in the near-IR, as opposed to the results here. We discuss a possible scenario where an episodic, one-off anisotropic acceleration formed a polar-fast and equatorially slow velocity distribution, having led to an effectively flaring geometry as we observe.

Unified Astronomy Thesaurus concepts: Black holes (162); Long baseline interferometry (932); Active galaxies (17)

1. Introduction

With long-baseline infrared interferometry, it is possible to spatially resolve the thermal emission from nuclear structures on subparsec scales in the nuclei of active galaxies (Active Galactic Nuclei, or AGNs). Such AGNs are thought to comprise a supermassive black hole surrounded by optically thick material that obscures the sight of the central putative accretion disk and ionized gas if viewed from an equatorial direction, while this nucleus can be directly seen along the polar direction (Antonucci & Miller 1985). The latter polar-viewed objects are believed to be Type 1s, while the former equatorially viewed ones are thought to be Type 2s. This system of optically thick, dusty material has been called a "torus."

Mid-infrared (mid-IR) interferometry explores the relatively outer region of the torus where the temperature of dust grains heated by the nucleus is $\sim\!300$ K, while the interferometry in the near-IR can probe the innermost dusty structure where dust grains are almost at the sublimation temperature of $\sim\!1500$ K. Here in this paper, we focus on this innermost region. For its exploration, the most suitable objects would be Type 1 AGNs, where the innermost region is directly seen without significant

Original content from this work may be used under the terms of the Creative Commons Attribution 4.0 licence. Any further distribution of this work must maintain attribution to the author(s) and the title of the work, journal citation and DOI.

obscuration and without much complication and confusion from dust extinction.

However, the overall angular size of the Type 1 nuclei turned out to be quite small. The innermost dusty region, or the dust sublimation region, is expected to be larger for brighter objects (the angular size would roughly be proportional to the square root of apparent flux; e.g., Figure 5 of Kishimoto et al. 2007), but even in the brightest Type 1 source on the sky, NGC 4151, the region is only partially resolved with the Keck interferometer's (hereafter KI) 85 m baseline (i.e., it shows only a small decrease of visibility; Swain et al. 2003; Kishimoto et al. 2009; Pott et al. 2010). Other Type 1 AGNs are also only partially resolved with Very Large Telescope Interferometer (VLTI) baselines up to 130 m (Weigelt et al. 2012; GRAVITY Collaboration et al. 2020; Leftley et al. 2021).

Another way to measure the radius of the dust sublimation region is to detect the time lag of the near-IR emission variation with respect to that of the nuclear optical emission (Koshida et al. 2009 and references therein), which has been very successful. The interferometric radii inferred from the small visibility decrease described above are in fact consistent with the time-lag radius where the interferometric radii, which are brightness-weighted radii giving the overall size of the dust sublimation region, are slightly larger than the near-IR reverberation radii, which are response-weighted and provide the inner boundary radius (e.g., Kishimoto et al. 2009, 2011a; for NGC 4151, the

Table 1Observed Visibilities for NGC 4151 at CHARA/CLASSIC in *K'* Band

Observing Date (UT)	Time (UT)	Telescopes	Projected Baseline (m)	Baseline PA (°)	V^2	$V^2 \text{ corr. for}$ $f_{AD} = 0.16 \pm 0.05$
2020-02-15	09 ^h 21 ^m	S1-S2	33.9	179.0	0.87 ± 0.15	0.85 ± 0.17
2020-02-16	08 ^h 19 ^m	S1-S2	33.9	7.3	1.00 ± 0.27	1.00 ± 0.33
2021-03-19	07 ^h 44 ^m	S2-W1	249.1	142.2	0.25 ± 0.08	0.17 ± 0.08
2021-04-30	05 ^h 18 ^m	S2-W1	249.4	139.1	0.36 ± 0.09	0.28 ± 0.10
2021-04-30	$08^{h}30^{m}$	S2-W1	216.6	113.3	0.63 ± 0.07	0.57 ± 0.08
2021-04-30	09 ^h 23 ^m	S2-W1	193.2	107.4	0.57 ± 0.15	0.50 ± 0.16

interferometric radius is \sim 0.5 mas, while the time-lag radius corresponds to \sim 0.3 mas; see Figures 3 and 4 in Kishimoto et al. 2013). If this interferometric size estimate is really correct, the observations with much longer baselines would reveal a large decrease of visibility, showing a definitely resolved structure. Here, we present observations of NGC 4151 with the CHARA Array at \sim 250 m baselines, a factor of \sim 2 longer than previously achieved for AGNs, or any other extragalactic objects, in fact. We show that the near-IR visibility goes down significantly at this long baseline, and we argue that we started to see morphological information on this target.

2. Observations

We have observed NGC 4151 with the CHARA Array (ten Brummelaar et al. 2005) over several different nights as summarized in Table 1. We used two baselines—a short, \sim 34 m baseline using the telescopes S1 and S2 in 2020, and a long, \sim 250 m baseline with telescopes S2 and W1 in 2021. On all occasions, the telescopes were equipped with an adaptive optics (AO) system, which has been commissioned recently. The details and operations of the CHARA Array AO system are described by ten Brummelaar et al. (2018) and Anugu et al. (2020), while the early design of the AO system is described by Che et al. (2013). We used the instrument CLASSIC, a twobeam combiner that is the most sensitive to faint targets among the various instruments at the CHARA Array. We used three different calibrators listed in Table 2, which are very close in projected distance to NGC 4151. They vary in optical and infrared magnitudes, with TIC9453648 closest in optical magnitude to NGC 4151. The science target was bracketed by calibrator observations close in time (except for the observation on 2020 February 15, when the time interval for one of the calibrator observations was long; see the Appendix). We observed them all in the K' band ($\lambda_{\rm obs} = 2.13 \,\mu{\rm m}$), not spectrally dispersed. The details of the sequences and raw visibilities observed are shown in the Appendix.

3. Data Processing

The data were processed following the steps described by Ten Brummelaar et al. (2013). The instrument CLASSIC scans each fringe with a dithering mirror. For NGC 4151 and all calibrators, we needed to scan relatively slowly, taking about 1.5 s to scan over $\sim\!70~\lambda_{\rm obs}$ (scanning frequency of $\sim\!250$ Hz, five samples per fringe, scanning over 150 $\mu{\rm m}$). After subtracting an averaged sky scan (scan of nearby sky region, which is regarded as a "dark" frame) from each scan, we first normalize each target scan by its low-pass-filtered version. Then we Fourier-transform the normalized scan to measure its fringe power by computing the power spectrum. The noise bias has been subtracted using the average power spectrum of the off-fringe scans.

Name	V (mag)	K (mag)	r _{proj} (°)	Diameter (mas) ^a
HD 105881	8.0	7.0	0.3	0.161 ± 0.004
SAO62878	9.8	8.3	0.09	0.092 ± 0.002
TIC9453648	11.6	8.7	0.2	0.090 ± 0.002

Note.

We have constructed our own IDL scripts to implement these steps, and calculated 10-scan, or 15 s, averages of squared visibilities V^2 over each fringe track, which lasted about 10 minutes each (5 minutes on fringe + 5 minutes off fringe). This confirmed the overall stability of the fringes, but also clearly identified certain tracks where fringes were within the scan range only in some portion of the track. In these cases, we only used one continuous range per track where fringes are visible in the V^2 track. Then we integrated all the power spectra from each track (or the designated range of the track) to calculate the final raw V^2 and also its uncertainty from the fluctuation of the raw V^2 over the track. The fluctuation of the off-fringe scans is also calculated and added in quadrature to the raw V^2 uncertainty. The system visibility for each observation of NGC 4151 was determined from the adjacent measurements of calibrators. Finally, we obtained the final calibrated visibility by dividing the raw V^2 with the estimated system visibility. The details of these processing and raw V^2 tracks are shown in the Appendix.

4. Results

4.1. Visibility versus Baseline

Figure 1 shows all the calibrated squared visibilities V^2 measured at short (\sim 34 m) and long projected baselines (\sim 190–250 m) with the CHARA Array, together with the previous measurements using the Keck interferometer (KI; Swain et al. 2003; Kishimoto et al. 2009, 2011a, 2013; Pott et al. 2010).⁸ The KI measurements only showed a hint of V^2 decrease as a function of baselines with only a small range of projected baseline lengths. Thus, the data did not rule out the case where there is an unresolved source of a high flux fraction (\sim 90%) with the rest of the flux coming from a large-scale structure. On the other hand, for different Type 1 AGNs, VLTI

^a Diameters from SearchCal by JMMC.

⁸ We have VLTI/AMBER data for NGC 4151 taken in 2012 as shown in Kishimoto et al. (2013), but we do not include them in our analysis here, because the VLTI/AMBER data might be affected by the coherence loss due to AO performance, which we now fear has not been quantified well. However, the radius measurement for 2012 is represented by our KI measurements in 2012, which we include here. The radius implied by the combination of KI and VLTI data is consistent with the one by KI, as quantified in Table 1 of Kishimoto et al. (2013).

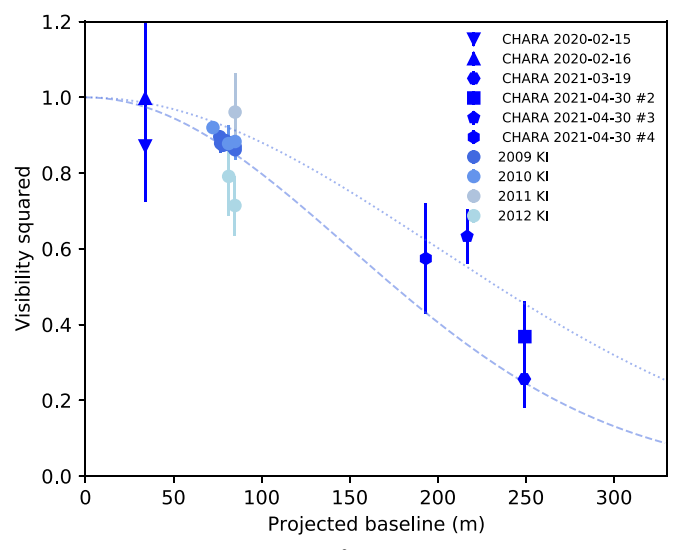


Figure 1. Observed visibility squared V^2 as a function of projected baselines. In addition to our CHARA Array data at ~ 30 m and $\sim 200-250$ m baselines, we also plotted visibilities observed at Keck interferometer (Kishimoto et al. 2013 and references therein). V^2 for Gaussian with HWHM of 0.3 and 0.4 mas are also plotted for reference in dotted and dashed curves, respectively.

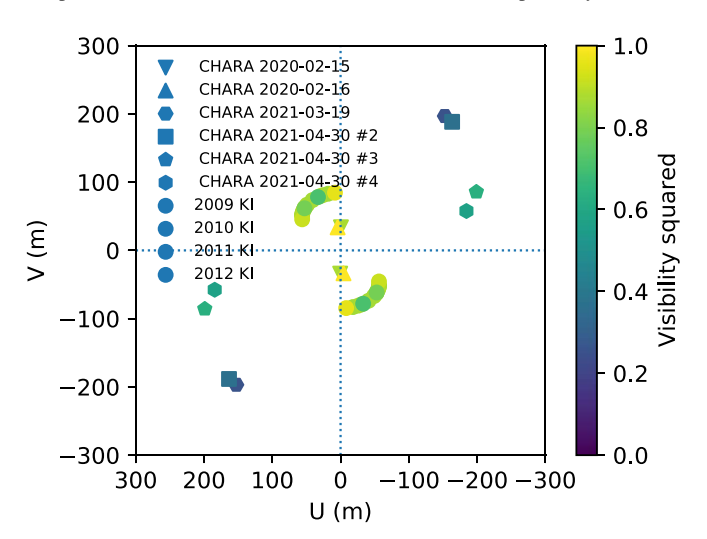


Figure 2. Sampled uv points, color-coded with observed visibility squared.

instruments AMBER and GRAVITY have shown that the visibilities decrease slightly over a wider range of baselines from ~40 to 130 m (Weigelt et al. 2012; GRAVITY Collaboration et al. 2020). Here, we show that the visibility does actually decrease significantly at long baselines in NGC 4151, establishing that we are definitely resolving the structure spatially.

4.2. Position Angle Dependence

The CHARA Array measurements reported here and the existing KI measurements for NGC 4151 are in fact complementary in the coverage of the position angle (PA) of the projected baselines. Figure 2 shows the uv coverage of all the observations, color-coded with the measured V^2 .

First, the four data points at $190-250\,\mathrm{m}$ baselines obtained with the CHARA Array actually suggest a dependency of V^2 on the PA, in the sense that the structure seems to be a bit more compact at PA $\sim 110^\circ$ than at $\sim 140^\circ$. To further investigate this, we show in Figure 3 the implied thin-ring radius for each V^2 measurement along the PA of the baselines for the CHARA

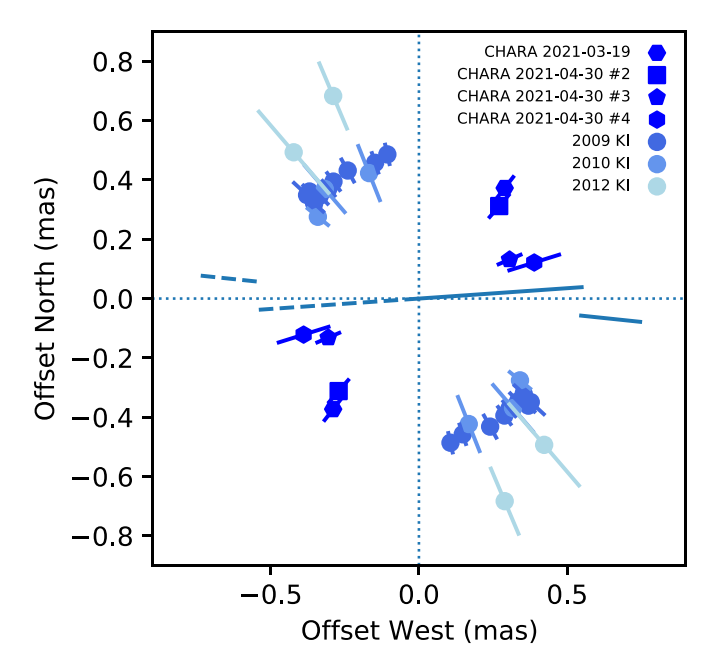


Figure 3. Thin-ring radius implied by each visibility observed (after the small correction for the putative AD component), plotted along the PA of the corresponding baseline. The PA of the optical polarization (94°), indicative of the system polar axis, is shown as the inner dashed–solid line, while the PA of the linear radio jet structure (84°; components D1/D2/D3 over 50 mas scale; Mundell et al. 2003) is indicated with the outer dashed–solid line segments.

Table 3
Thin-ring Fit Results

	Radius (mas)	min/maj	PA (°)
All data	0.462 ± 0.050	0.74 ± 0.10	19 ± 10
CHARA + 2012 KI	0.669 ± 0.086	0.46 ± 0.08	25 ± 6
All data with	0.507 ± 0.047	0.74 ± 0.09	17 ± 10
$f_{\rm AD} = 0.16 \pm 0.05$			

Note. For the KI data, we incorporate the conservative systematic uncertainty of 0.03 in V^2 (Section 3.2 in Kishimoto et al. 2011a).

Array measurements, as well as the KI measurements (see below for further details on the corrections implemented). The three V^2 data points, which are consistent with unity within uncertainties, are not shown in this plot, since they do not give meaningful radius constraints alone. As a whole, we seem to see a moderate elongation along roughly a north–south direction.

Here, we have chosen to use a thin-ring model rather than a Gaussian geometry, since the central part is considered devoid of dust emission, due to dust sublimation (see more discussions in Section 5.4). We are still unable to differentiate these geometries from the data themselves, which are within the first lobe of the visibility curve. The ring is adopted to be infinitely thin, to minimize the number of parameters involved.

Furthermore, we do expect that the central part, even if devoid of dust emission, has another thermal emission component from the putative accretion disk (AD). Based on the optical to near-IR spectral energy distribution, this has a fractional flux contribution at *K*-band $f_{\rm AD}$ of $\sim 0.16 \pm 0.05$ for NGC 4151 (Kishimoto et al. 2013 and references therein). Therefore, assuming that this component remains unresolved, we calculated the V^2 for the dust emission component (quoted in Table 1) and the corresponding thin-ring radii. These are the radii shown in Figure 3.

In Table 3, we show the results of the thin-ring fit to the whole V^2 data set, both for the simple ring and AD-corrected

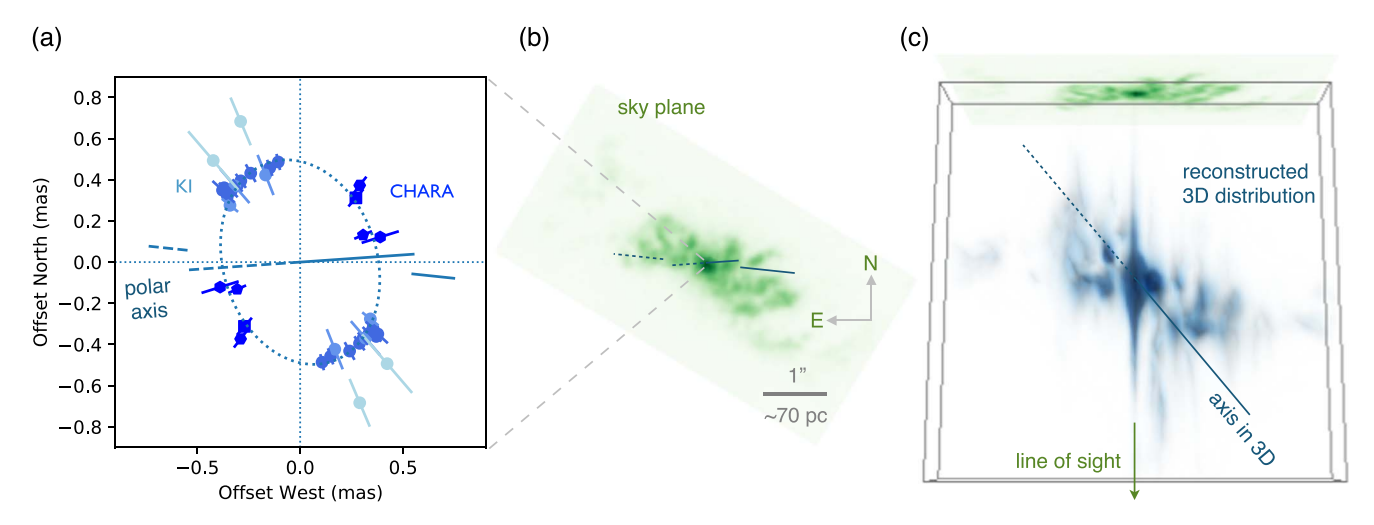


Figure 4. (a) The same ring radii as in Figure 3 but with the fitted thin-ring model shown in dotted line. The inner dashed–solid line indicates the polar axis as probed by the optical polarization, and the outer dashed–solid line segments show the PA of the radio jet, exactly the same as in Figure 3. (b) HST/WFPC2 archival image of the narrow-line region in [O III]5007 line, with the two sets of dashed–solid line segments corresponding to those in panel (a). (c) Three-dimensional distribution of [O III]-emitting clouds reconstructed from HST/STIS multi-slit data, which cover the volume indicated by gray lines. For reference, the HST image from panel (b) in green is also shown at the back of the 3D cube, as the 2D flux distribution projected on to the sky plane. This is as seen almost perpendicular to our line of sight. An approximate axis of this 100 pc scale conical structure is indicated in a dashed–solid line.

ring fit (note the difference is only $\sim 10\%$). The latter is shown in Figure 4(a) as a dotted line, on top of the same ring radii as shown in Figure 3. The projected ring has its major axis at a PA of $17^{\circ} \pm 10^{\circ}$ with a radius 0.507 ± 0.047 mas. The minor-to-major axis ratio is 0.74 ± 0.09 , thus showing an elongation.

The lack of baseline length coverage between 90 and 190 m leaves some uncertainty in the geometric fit to reproduce the data. An alternative would be a power-law brightness distribution with a certain inner cutoff, a distribution that is more extended in the outer region and more compact in the inner region. However, we found that such a shallow power-law fit to the observed visibilities yields an inner cutoff radius that is too small, which would be inconsistent with the measured time-lag radius (see Section 1). Therefore, despite the baseline gap, the adopted thin-ring model seems quite adequate in measuring the overall size and elongation direction of the brightness distribution.

5. Discussions

5.1. System Axis Direction and Equatorial Elongation

The system axis direction of the nucleus of NGC 4151 can be inferred from a few different observations. At a few arcsec scale, Hubble Space Telescope (HST) images show that the narrow-line region is extended roughly along an E-W or NE-SW direction as shown in Figure 4(b), indicating that the polar axis of the system is along this direction. A more accurate reference at a slightly smaller spatial scale is the linear jet-like structure observed at radio wavelengths. The one arcsec scale radio map clearly shows a linear structure roughly extended along E-W direction, with some systematic wiggles along the structure (Mundell et al. 2003). In the innermost region, where component D is considered to have the active nucleus (Mundell et al. 2003; Ulvestad et al. 2005), the structure is linearly extended along ${\sim}84^{\circ}$ over ${\sim}50$ mas scale at ${\sim}10$ mas resolution (Mundell et al. 2003). The brightest subcomponent D3 has been shown to also be extended roughly along the same direction at a \sim 1 mas resolution (Ulvestad et al. 2005; see Section 5.6).

The reference for the axis direction at an even smaller scale is from optical spectropolarimetry. NGC 4151 shows an optical polarization of $\sim 1\%$, with its PA parallel to the linear jet direction, which is quite typical for Type 1 AGNs (Antonucci 1983). The polarization is believed to originate from electron scattering in an optically thin, equatorial region (Antonucci 1983; Smith et al. 2004; Lira et al. 2020), located somewhere between the broad-line region (or co-spatial with the broad-line region) and dust sublimation region. Thus, in terms of the spatial scale, this is probably the most suitable reference. The polarization seems to be variable, namely at 91° and 97°, observed ~ 2 yr apart (1992/1994–1995; Martel 1998).

These directions are graphically shown in Figure 3; the inner dashed–solid line indicates the polarization PA (at 94° , the average of the two above), while the outer dashed–solid line segments corresponds to the linear jet direction. The same directions are shown also in Figures 4(a) and (b). If we consider a roughly axisymmetric structure, these directions are supposed to indicate the polar axis direction of the system. Therefore, the elongation observed with the near-IR interferometry (the thinring fit is shown in Figure 4(a)) is approximately perpendicular to this system axis, implying that the near-IR continuum emitting region looks rather elongated along the equatorial direction of the system.

5.2. Size Variability

Due to the variability of the nuclear luminosity, the radius of the dust sublimation region could vary over the years. The radius of the near-IR emitting region in NGC 4151 has been claimed to show variation both in the near-IR reverberation (Minezaki et al. 2004; Koshida et al. 2009; Schnülle et al. 2015) and interferometry (Kishimoto et al. 2013). Pott et al. (2010) pointed out no significant increase in interferometric radii against the flux increase by a factor of 2, while Kishimoto et al. (2013) argued that the radius change might be occurring as a function of the averaged AD flux over several years. On the other hand, Schnülle et al. (2015) showed that the time-lag radius decreased as opposed to the interferometric radius increase. If the radius does vary, however, it might not be

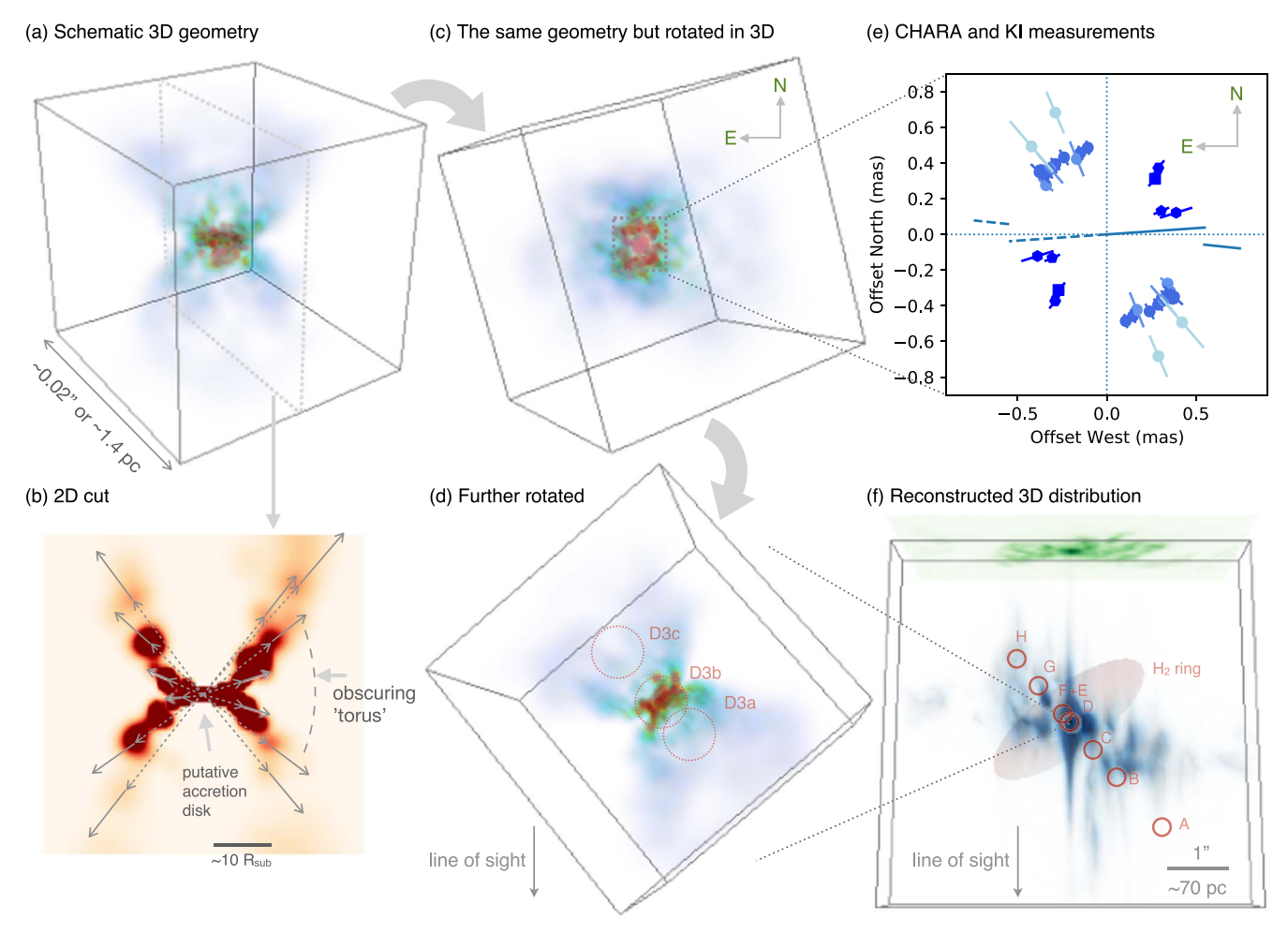


Figure 5. (a) Schematic 3D geometry inferred for the central region (reproduced from Figure 8(b) in Miyauchi & Kishimoto 2020). (b) 2D cut of the 3D geometry shown in panel (a) (reproduced from Figure 8(d) in Miyauchi & Kishimoto 2020 with additional annotations). (c) The same geometry as in panel (a), but rotated in 3D to match the possible configuration in NGC 4151 as seen from our perspective, where the central dotted square schematically corresponds to the region mapped by the CHARA Array and KI as indicated in panel (e), which is the same as Figure 3. (d) The same 3D geometry, but further rotated to a side view, perpendicular to our line of sight to the object. Approximate 3D locations inferred for the VLBI components (15 GHz; Ulvestad et al. 2005) are schematically shown in red circles. (e) See the description for panel (c). (f) Reconstructed 3D distribution shown in Figure 4(c), but with approximate 3D positions inferred for knots A–H of the radio jet (Mundell et al. 2003). The molecular hydrogen distribution as inferred by Fernandez et al. (1999) is shown as a red transparent ring in 3D with inner and outer radii of 0.15 and 1.15.

adequate to compare KI and CHARA data here, given that the KI and CHARA observations are separated in time by over $\sim\!10~\text{yr}.$

To quantify its potential effect, we have estimated the current expected size based on the prescription for the variability given in Kishimoto et al. (2013), where the size is not determined by the instantaneous nuclear flux, but it varies as a function of its long-time average (because the size variation would depend on the timescale of dust sublimation and dust formation). We supplemented the light curve shown in Figure 3 of Kishimoto et al. (2013) with the monitoring data available from AAVSO⁹ for NGC 4151 over the last \sim 10 yr, and calculated the suggested 6 yr flux average. The flux has been relatively steady since the last high state occurred around 2011, and the resulting predicted size at the current period is calculated to be roughly the same (within \lesssim 5%) as that in 2012. We have then implemented a thin-ring fit to the CHARA data only with the 2012 KI data (i.e., exclude the ones from 2009 to 2011). The results are shown in Table 3. The minor-to-major axis ratio becomes smaller, but the elongation PA does not change significantly, so

the elongation direction still seems roughly perpendicular to the system axis.

5.3. Inclined Ring and Inclination Angle

The near-IR continuum emission at $\sim 2~\mu m$ is believed to be predominantly from the innermost, hottest dust grains almost at the sublimation temperature. We tend to consider these sublimating dust grains to be concentrated in the equatorial plane of the system, probably slightly outside the broad-emission-line region. The elongation observed above is consistent with such a naive expectation. In this case, we can formally derive the inclination angle from the ellipticity of the elongation, assuming that the region has a ring-like structure. From the minor-to-major axis ratio of the thin-ring fit described above (Figure 4(a)), we would infer an inclination angle of $\sim 43^{\circ} \pm 6^{\circ}$.

We can compare this value with other estimations from different data sets. Among others, Das et al. (2005) deduced an inclination angle of $45^{\circ} \pm 5^{\circ}$ by modeling the HST/STIS multi-slit data with a conical hollow outflow model over a 100 pc scale region. The modeling is based on the assumption of a "linear" outflow where the velocity of clouds are radial in

http://www.aavso.org

direction and linearly proportional to the distance from the nucleus. In fact, if we adopt the same velocity field, the distribution of line-emitting material in three-dimensional space can directly be reconstructed from the data, as shown by Miyauchi & Kishimoto (2020) for a similar HST/STIS data set for the Seyfert 2 galaxy NGC 1068. Here, we have implemented the same 3D reconstruction using the data set of Das et al. (2005) for NGC 4151. The result is shown in Figure 4(c). Details are described elsewhere, but the 3D distribution visualizes and illustrates the possible configuration of the material at a 100 pc scale, or 1" scale. Consistent with the modeling of Das et al. (2005), it shows a patchy but approximately hollow and conical distribution, and it does suggest an inclination consistent with the value inferred from the assumption of an equatorial ring for the interferometry data. The SW side is the conical outflow toward us, as deduced by Das et al. (2005). It is quite striking that the 100 pc scale structure and the much smaller-scale structure probed by our CHARA Array observations suggest similar inclinations.

5.4. Why in an Equatorial Plane?

In the mid-IR, long-baseline interferometry has shown that many objects have polar-elongated morphology at pc scales, or tens of R_{sub} scales, where R_{sub} is the dust sublimation radius (Hönig et al. 2012, 2013; López-Gonzaga et al. 2014, 2016; Tristram et al. 2014), though the mid-IR interferometry data for NGC 4151 are not clear about this point, because the PA coverage of the data is poor (Kishimoto et al. 2011b; Burtscher et al. 2013). On the other hand, the mid-IR interferometry for large angular size AGNs (i.e., NGC 1068 and Circinus galaxy) indicates an equatorial elongation in several R_{sub} scales, embedded in the polar elongation at much larger scales of tens of R_{sub} (Raban et al. 2009; López-Gonzaga et al. 2014; Tristram et al. 2014). This has now even more clearly been shown by mid-IR interferometric imaging for NGC 1068 (Gámez Rosas et al. 2022; see more below) and for Circinus (Isbell et al. 2022). Since we are probing a few $R_{\rm sub}$ scale for NGC 4151 here ($\lambda/b \sim 1.8$ mas; $R_{\rm sub} \sim 0.3-0.5$ mas for NGC 4151), our detection of the equatorial elongation seems geometrically consistent with such a structure being seen by the mid-IR interferometry.

In fact, with the near-IR interferometer VLTI/GRAVITY, Leftley et al. (2021) has detected an equatorial elongation in the near-IR for the Type 1 AGN ESO323-G77, despite the small visibility decrease at baselines up to 130 m. The object shows a polar elongation in the mid-IR (Leftley et al. 2018). Thus, the equatorial elongation as seen by the CHARA Array for the Type 1 AGN NGC 4151 seems to fit in with all these interferometric results.

The polar-elongated morphology found in the mid-IR at the pc scale, combined with the larger-scale HST-resolved outflow, would suggest a conical and hollow outflowing structure also at the inner pc scale. This wind has been suggested to be driven by the radiation pressure on dust grains (Hönig et al. 2012, 2013). In this case, it is likely to be launched at the dust sublimation region. There, the dusty gas could be inflated or puffed up by the infrared radiation of the heated grains (Krolik 2007), and then be radially accelerated by the UV radiation from the nucleus and form the hollow conical structure (Honig 2019). This near-IR emitting, wind-launching region might seem to be a distinct, separate component in the spectral energy distribution (e.g., Mor et al. 2009; Kishimoto et al. 2011b;

Hönig et al. 2012), and in particular, this could correspond to the bump-like feature at around 3 μ m seen in the spectra of many Type 1 AGNs (Hönig & Kishimoto 2017). Regarding this near-IR emitting region as a slightly extended disk and the mid-IR emitting component as a dusty wind, the model of Hönig & Kishimoto (2017) has successfully explained the near-IR and mid-IR observations of the Type 1 AGNs NGC 3783 and ESO323-G77 including interferometry (Leftley et al. 2021).

However, the observed emission properties of the 100 pc scale outflow, the pc scale polar elongation, and the subpc scale equatorially elongated structure might actually suggest that all these three originate from the same nuclear wind. They are all rather continuously distributed on the plane of the surface brightness and color temperature (Figure 7 in Miyauchi & Kishimoto 2020). We can also estimate the infrared emissivity (i.e., surface brightness in units of Planck function) of these components on this plane, and infer the optical thickness. While the 100 pc scale outflow is UV-optically thin, the pc scale structure (showing the polar elongation in the mid-IR) seems UV-optically thick. This means that this inner hollow outflow would provide the obscuration of the nucleus in equatorial directions in the UV/optical, as also argued by Honig (2019). In this case, the whole outflow would be the obscuring "torus," and we would not need to invoke the disk component for obscuration described above. The near-IR emitting component would not be a distinct one, but instead would simply be the innermost part of the outflow. But then, we would rather expect that it would look more polar-elongated, as opposed to the CHARA Array results presented here.

5.5. Flaring Geometry from Episodic, One-off Acceleration

One consistent picture might be that the distribution actually is effectively geometrically flaring (see Figure 5(a)), with the cloud acceleration being one-off, or episodic, rather than continuous. The geometrical flaring would give an inner-equatorial, outer-polar structure, explaining the mid-IR interferometry results for NGC 1068 and Circinus described above with a single structure (i.e., it explains the two components of the inner-equatorial and outer-polar structures as a single entity) and the CHARA Array results at the same time. Here, we do not infer that each cloud follows the flaring path, as it would need an additional acceleration toward the polar-axis direction in the outer radii. Rather, in fact, it has been argued that the velocities of the outflowing clouds at 100 pc scales could be from a one-off, episodic acceleration (once in $\gtrsim 10^5$ yr) at the innermost wind-launching site, since they are Hubble-flowlike, i.e., the velocity of each cloud seems proportional to its distance to the nucleus (Ozaki 2009; Miyauchi & Kishimoto 2020). The flaring geometry above can be realized if each cloud is simply moving radially at a roughly constant speed but the clouds have a polar-fast, equatorially slow velocity distribution from the one-off anisotropic acceleration (see Figure 5(b)), which might be reasonable for the radiation pressure from an accretion disk.

This possible episodic acceleration might actually be quite consistent with the episodic activity that has been inferred from X-ray observations. Wang et al. (2010) have identified a significant soft X-ray emission extended out to $\sim 10^4$ lt-yr from the nucleus of NGC 4151. This emission has been interpreted to indicate either mechanical heating by an episodic outflow or photoionization by a highly luminous, Eddington-limited outburst. In both cases, the episodic activity is estimated to have

occurred in the last 10^4 – 10^5 yr, which is a timescale quite similar to what we discuss here.

The flaring geometry from an episodic acceleration (Figure 5(a)) as seen edge-on might fit with the mid-IR interferometric image in Gámez Rosas et al. (2022) (their Figure 1(e), mid-IR RGB-composite image). The illustration in Figure 5(a), which is from Figure 8 in Miyauchi & Kishimoto (2020), is intended to represent the distribution of the ionized gas and $T \ge 300 \text{ K}$ dust, and the inner equatorial region (represented in red) would correspond to the near-IR emitting, dust sublimation region. This might also be consistent with the 3.7 μ m image in Gámez Rosas et al. (2022) showing an equatorial structure, with the dust sublimation region being still hidden below. In the case of the Type 1 object NGC 4151, we would see the sublimation region directly—Figure 5(c) shows the same 3D illustration, but rotated in 3D to match the inferred inclination and PA of the axis projected on the sky for NGC 4151, with the central square schematically corresponding to the CHARA Array and KI observations (Figure 5(e)). This illustrates the possible configuration in NGC 4151. Figure 5(d) shows the same geometry further rotated to provide a view perpendicular to both our line of sight and the system axis, corresponding to the view of the reconstructed 3D distribution at a much larger scale shown in Figure 4(c) and reproduced in Figure 5(f).

5.6. Relations to Other Observations and Simulations

How would this structure be related to those observed at other wavelengths and other scales? As mentioned in Section 5.1, the radio continuum source D3, believed to contain the nucleus (Mundell et al. 2003), has been resolved at ~ 1 mas resolution with VLBI (a beam size of 0.95×0.46 mas; Ulvestad et al. 2005). The source is resolved into three components along the E-W radio jet direction. The middle component D3b is argued to be the nucleus, with the other two knots $\sim 1-2$ mas away from it. Thus, the dust sublimation region of ~0.5 mas in radius, as resolved by the CHARA Array observations here, would be located at the center of the three-knot jet-like structure that has a scale comparable to that of the sublimation region itself. This is schematically shown in Figure 5(d), where approximate 3D positions of the three knots are indicated. Here, the jet axis at this scale is assumed to coincide with the system axis, based on the inclination of $\sim 40^{\circ}$ inferred for the radio jet at larger scales (Pedlar et al. 1993), which is consistent with the inclination of the system discussed in Section 5.3.

At slightly larger, 10-100 mas scales, neutral hydrogen absorption is observed in one of the several components of the linear radio jet. This is the component called E + F, which is at the counter-jet side but closest to the radio nucleus D3 (the projected distance is \sim 70 mas or \sim 5 pc; Mundell et al. 1995, 2003). In Figure 5(f), we have drawn approximate 3D positions of the jet components, again assuming an inclination of 40°. In terms of the episodic polar-fast outflow discussed above, this foreground neutral hydrogen material in front of the counter jet component E + F might be a part of the slow-velocity outflows moving relatively close to equatorial directions. In the scenario of the one-off acceleration $\sim 10^5$ yr ago, the clouds several pc away from the nucleus would be at a velocity of several tens of km s⁻¹, which would be consistent with the observed radial velocities of the absorption lines (Figure 5(b) of Mundell et al. 2003).

This central region seems to be surrounded by a molecular ring-like structure at slightly outer radii of $\sim 1''$, which is observed in the infrared molecular hydrogen line H₂ 1–0 S(1), with a projected major axis PA $\sim 170^{\circ}$ and inclined by $\sim 37^{\circ}$ from our line of sight (Fernandez et al. 1999). This configuration is schematically shown in 3D in Figure 5(f) as a red transparent ring (inner and outer radii of 0."5 and 1."5, respectively). The kinematics of this ring is inferred to be dominated by rotation, rather than outflow, based on their Fabry-Perot image missing the north-south part, which would possess higher radial velocities if in rotation. Therefore, this ring might be kinematically distinct from the obscuring and outflowing torus discussed above, and instead be an outer part of the "fueling disk," an equatorial thin disk-like structure that transfers material toward the nucleus (Honig 2019; Miyauchi & Kishimoto 2020).

The idea of a wind being responsible for the obscuration of the nucleus has been investigated with theoretical calculations and numerical simulations. The obscuring wind could be from a combination of X-ray heating and radiation pressure (Krolik & Begelman 1986, 1988; Wada 2012), or as mentioned in Section 5.4, it could be triggered by IR radiation pressure from heated dust and accelerated by the AGN UV radiation (Krolik 2007; Chan & Krolik 2016, 2017; Dorodnitsyn et al. 2016; Namekata & Umemura 2016; Williamson et al. 2019, 2020). As for the episodic property, the hydrodynamical winds simulated by Wada (2012, 2015) are in fact quite intermittent in nature.

Here, we have argued observationally that an episodic wind accelerated by polar-strong radiation, forming an effectively flaring geometry, would be able to explain the near-IR equatorial elongation at an R_{sub} scale, mid-IR polar elongation at tens of R_{sub} scale, as well as the linear velocity field and the hollow conical outflow at a 100 pc scale, at least qualitatively.

While the exact physical processes for launching winds are still being explored theoretically, a modeling focused on reproducing these observed properties, including possible episodic acceleration, would enable us to do more quantitative comparisons with observations.

We plan to implement such modeling, as well as acquire further data on this innermost structure, with the CHARA Array.

6. Summary and Conclusions

We have presented the near-IR interferometric measurements of the Type 1 AGN NGC 4151 at projected baselines up to $\sim\!250$ m, the longest baseline achieved so far in the infrared for an extragalactic object. With these baselines, the compact near-IR structure, or the dust sublimation region, has now been spatially resolved. The measurements provide the size along different position angles, giving the first information on the morphology of the object at this inner spatial scale. When combined with the previous Keck interferometer data, albeit at shorter baselines, we find that the region is elongated along a roughly north—south direction, perpendicular to the system axis direction as determined by the linear radio jet structure and optical polarization observations.

We argued that an effectively flaring geometry can explain both the inner-equatorial and outer-polar elongation simultaneously, which are seen in our CHARA Array observations and by mid-IR interferometry. The flaring geometry at a given time could be formed from a polar-fast, equatorially slow, one-off acceleration, while the episodic acceleration is quite consistent with the Hubble-flow-like velocity field observed at a $\sim 100~\rm pc$ scale. Long-baseline measurements covering a wide position-angle range in a single epoch are now desired to confirm the results. We are now aiming for acquiring such data at the CHARA Array, which is currently the only infrared interferometer that has such long baselines and sufficient uv coverage.

This work is based upon observations obtained with the Georgia State University Center for High Angular Resolution Astronomy Array at Mount Wilson Observatory. The CHARA Array is supported by the National Science Foundation under grant No. AST-1636624 and AST-2034336. Institutional support has been provided from the GSU College of Arts and Sciences and the GSU Office of the Vice President for Research and Economic Development. We are grateful for all the generous and patient support from the CHARA staff members since the start of this project in 2010 at the CHARA Array. A part of the time at the CHARA Array was granted through the NOIRLab community access program (NOIRLab PropIDs: 2010A-0081, 2012A-0187, 2013A-0241, 2014A-0072, 2015A-0242, 2016A-0091, 2017A-0049, 2018B-0109, 2019A-0055, 2021A-0013; PI: M. Kishimoto). This work was supported in part by JSPS grants 16H05731, 20K04029 and 21H04496, and the grant E1906 through Kyoto Sangyo University. We gratefully acknowledge the variable star observations from the AAVSO International Database contributed by observers worldwide and used in this research. This research has made use of the Jean-Marie Mariotti Center Aspro and SearchCal services.

Appendix Observed Raw Visibilities and Power Spectra of Fringe Tracks

Figure 6 shows the raw visibilities for each calibrator and the target observed in the night of 2020 February 15. For each object, the raw visibilities obtained by averaging the power spectra over 10 scans (corresponding to an integration over ~ 15 s) are shown in dotted lines. The visibilities integrated over each track of calibrator observations are shown in filled blue circles with uncertainties. The open circles show the system visibilities (transfer functions) at the time of the calibrator

observations (almost overlapping with the calibrators' raw visibilities) and at the time of the science target observation. The latter is obtained from the linear interpolation between the system visibilities bracketing the science target observation. The visibility integrated over the track (or a portion of the track; see below) for the science target is shown in a green filled circle along with its uncertainty.

Figure 7 shows the details of the fringe track for NGC 4151 on 2020 February 15. The top left panel (a) shows the envelope (fringe amplitude) over each scan, in grayscale (note the rightside axis showing approximate elapsed time in seconds). The top middle panel (b) shows the corresponding power spectra, also in grayscale. Fringes should be detected at the frequency of one cycle per observing wavelength λ . They are clearly visible, with some wiggles around this frequency over different scans. The top right panel (c) shows the raw V^2 value for each scan in dotted lines, while the light blue dots correspond to the averages over 10 scans. In the bottom panel (d), the red dotted line is the final averaged power spectrum, with the same spectrum smoothed over 10 frequency pixels shown as a red solid line. This is after the subtraction of the noise bias spectrum, which is measured from the average of the same number of off-fringe scans as the object scans. Here, the power spectrum before the subtraction is shown in blue and the noise bias spectrum in gray, with the scale axis for both indicated at the right side in blue.

In this particular fringe track, the fringes slipped away from the scan range at and around scan #220. Therefore, we integrated the power spectra until scan #190. The integration range is indicated with a green vertical line in panel (c), with its x-axis position corresponding to the value of the obtained V^2 from the integration. The uncertainty is also shown in the horizontal green line at the midpoint of integration. Note that the exact choice of the scan number for integration does not alter the results beyond the estimated uncertainty.

Figures 8–16 show the observed raw visibilities in the same way. Multiple tracks of the science target within a given night are marked with sequential numbers, and shown individually in separate figures. Note that we did not see fringes in track #01 for NGC 4151 on the night of 2021 April 30. Because we are not entirely sure if the scans were in the right range, this track was excluded from the analysis, but it is shown here for completeness.

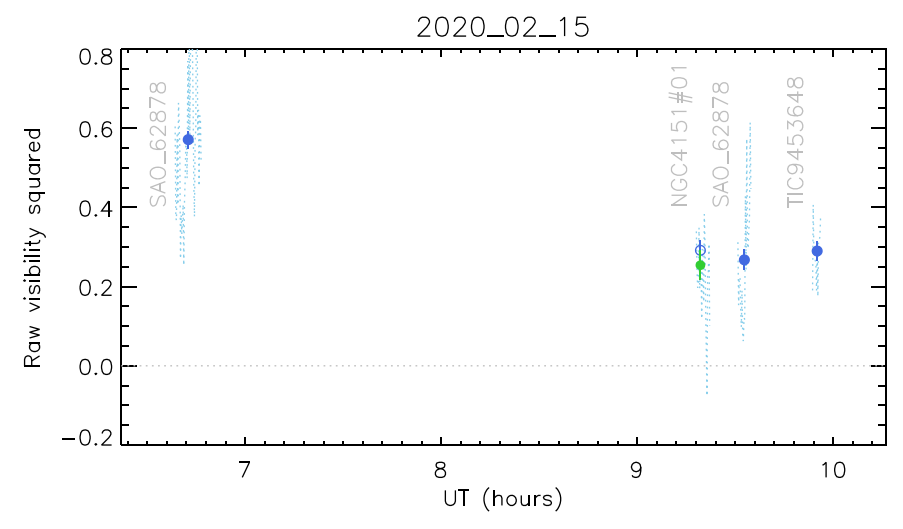


Figure 6. Observed raw visibilities in the night of 2020 February 15 at CHARA. Light dotted lines show the raw visibilities averaged over 10 scans (\sim 15 s) in each track of objects. Blue filled circles show the raw visibilities integrated over each track of calibrators with uncertainties. Blue open circles are the system visibilities estimated from the calibrator observations. The green filled circle is the raw visibility of the science target from the integration over the track.

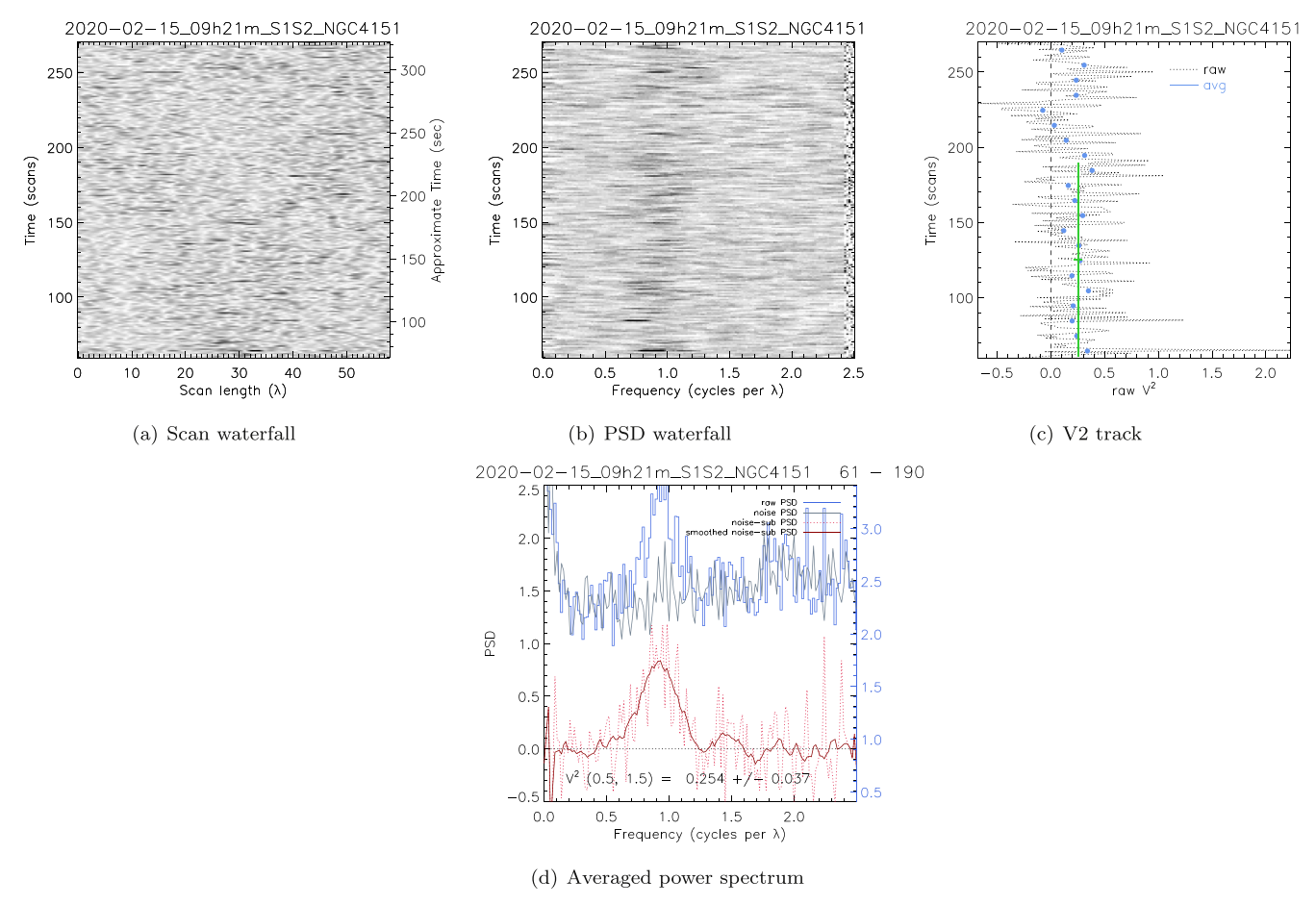


Figure 7. Details of the fringe track for NGC 4151 on 2020 February 15. (a) Fringe envelopes of the scans are shown in grayscale, with each scan in the horizontal direction, forming a waterfall plot along the vertical direction. (b) Power spectrum of each scan is shown in grayscale along the horizontal direction, again forming a waterfall plot of power spectra. (c) Dotted lines show the raw V^2 obtained from integrating each power spectrum, and the blue dots indicate its 10-scan average. (d) Averaged power spectrum is shown as a red dotted line, with its smoothed version indicated by a red solid line. The blue spectrum is before the subtraction of the noise bias, which is shown in gray, with the scale axis shown on the right side in the same shade blue color.

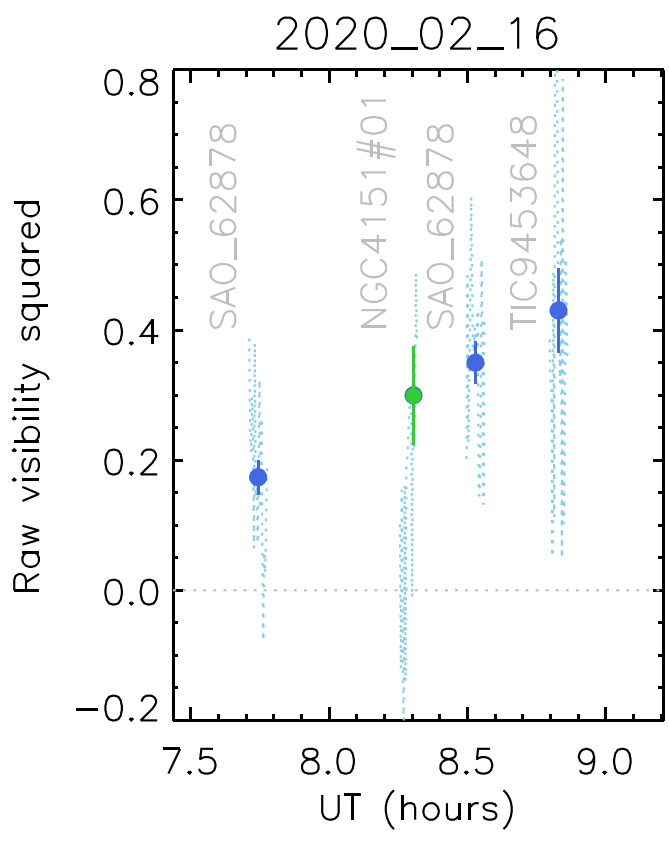


Figure 8. Observed raw visibilities in the night of 2020 February 16 at CHARA. The notations are the same as in Figure 6.

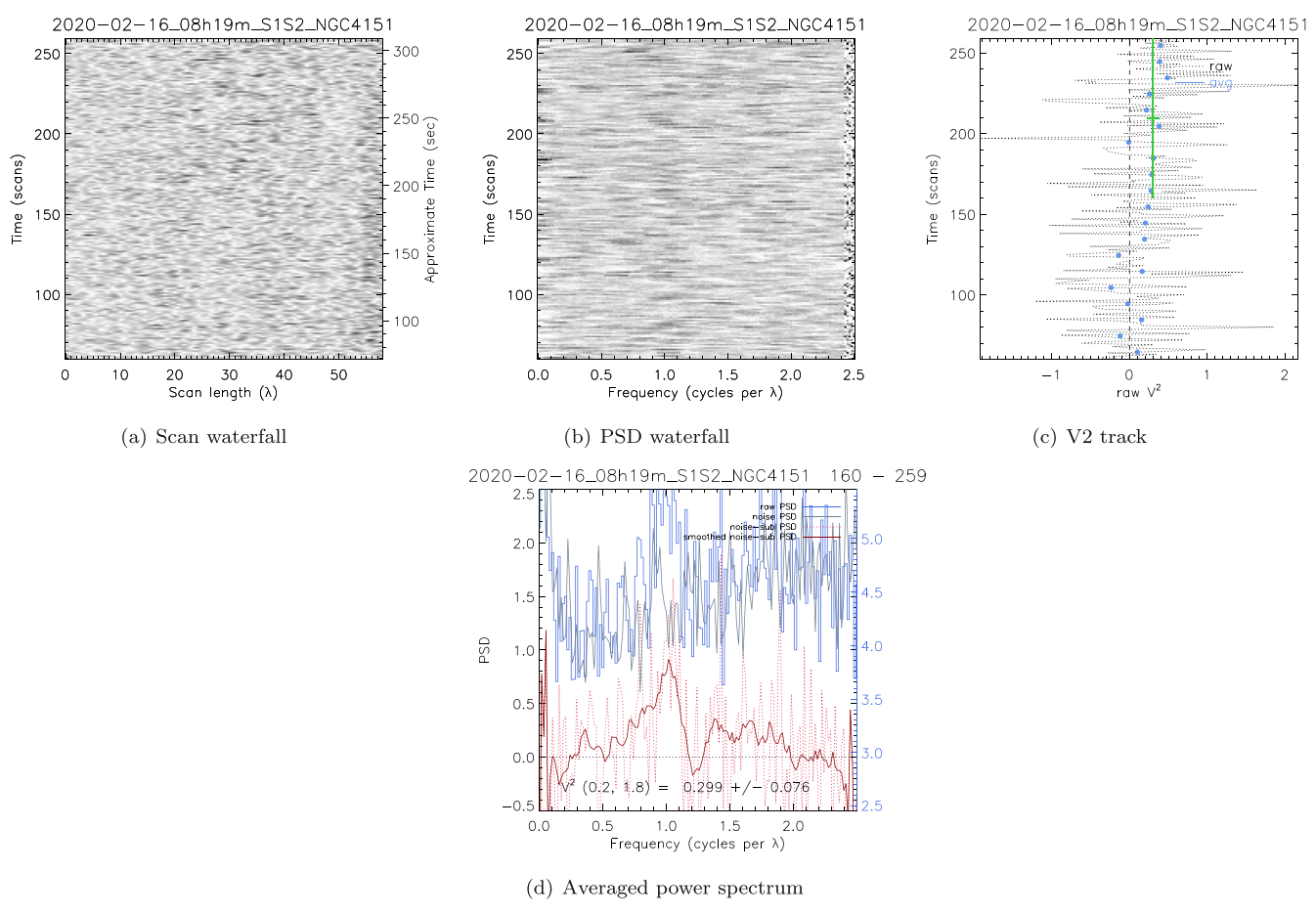


Figure 9. Details of the fringe track for NGC 4151 on 2020 February 16, in the same format as in Figure 7.

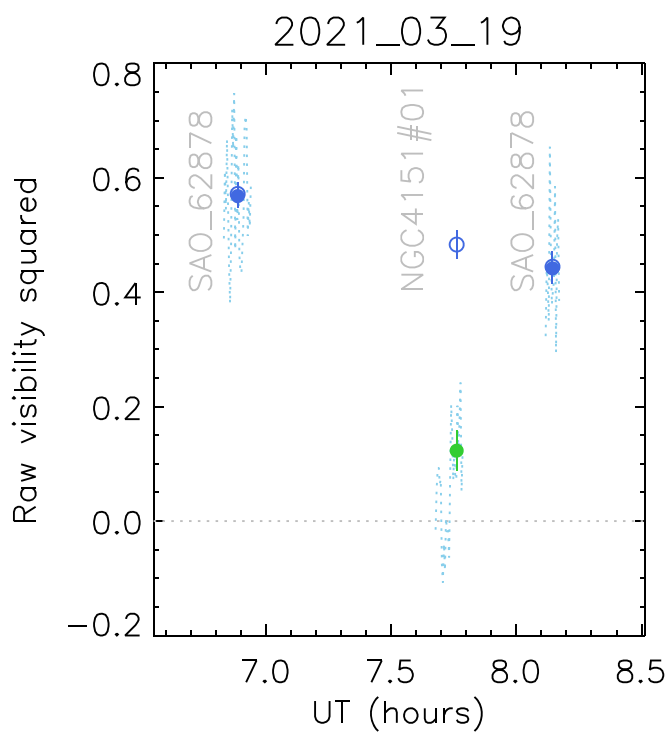


Figure 10. Observed raw visibilities in the night of 2021 March 19 at CHARA. The notations are the same as in Figure 6.

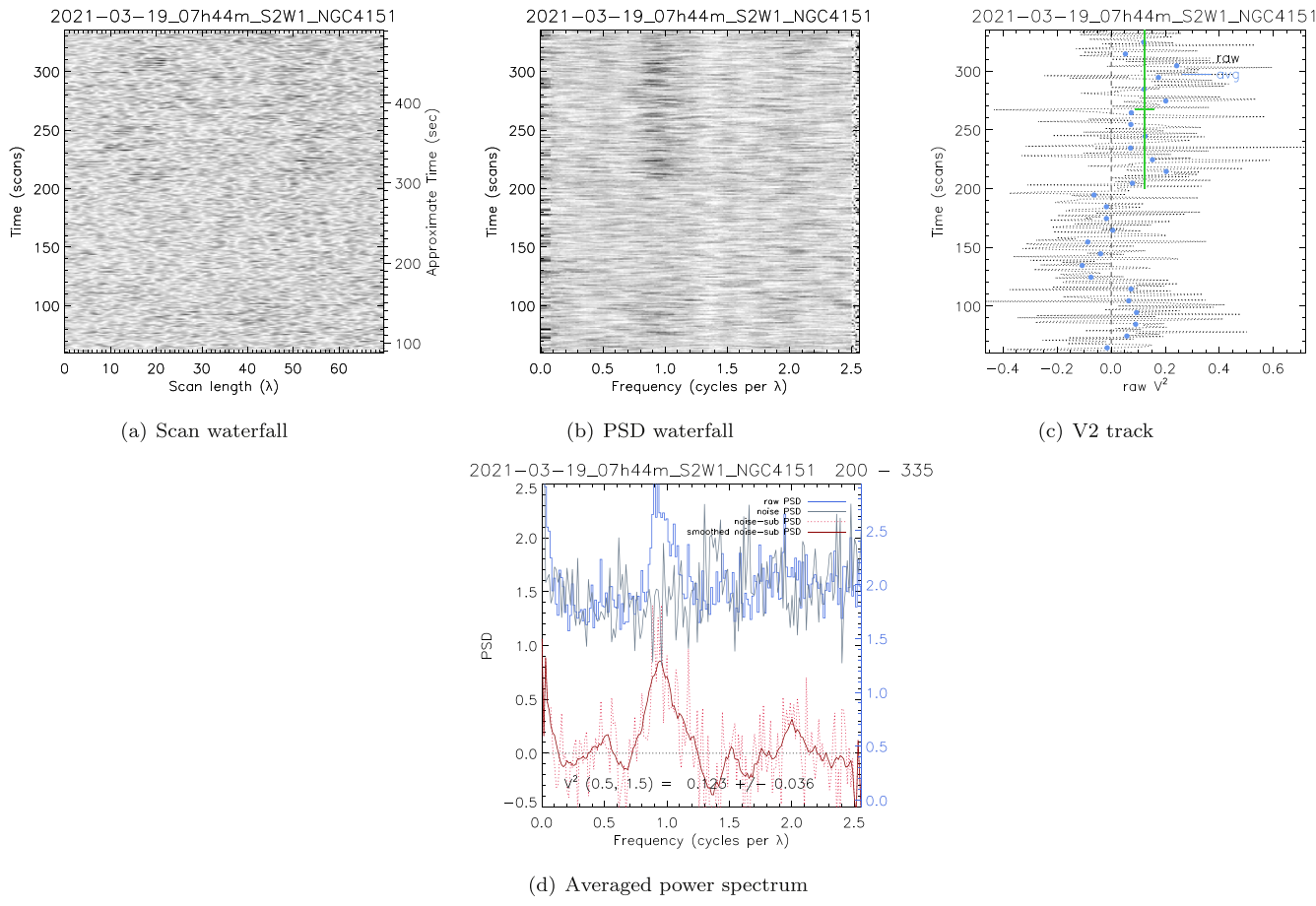


Figure 11. Details of the fringe track for NGC 4151 on 2021 March 19, in the same format as in Figure 7.

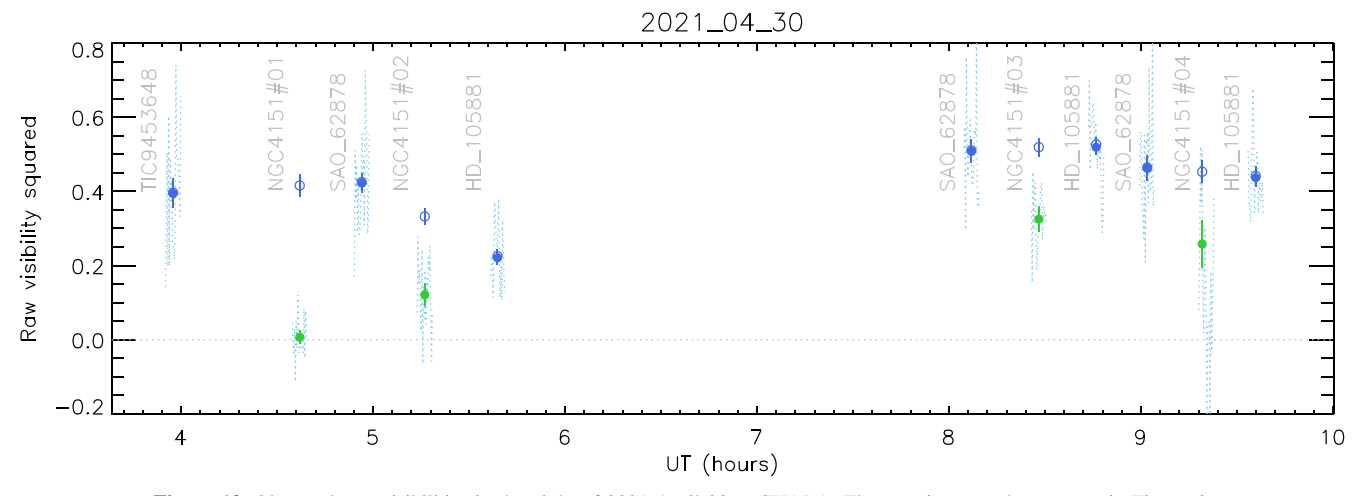


Figure 12. Observed raw visibilities in the night of 2021 April 30 at CHARA. The notations are the same as in Figure 6.

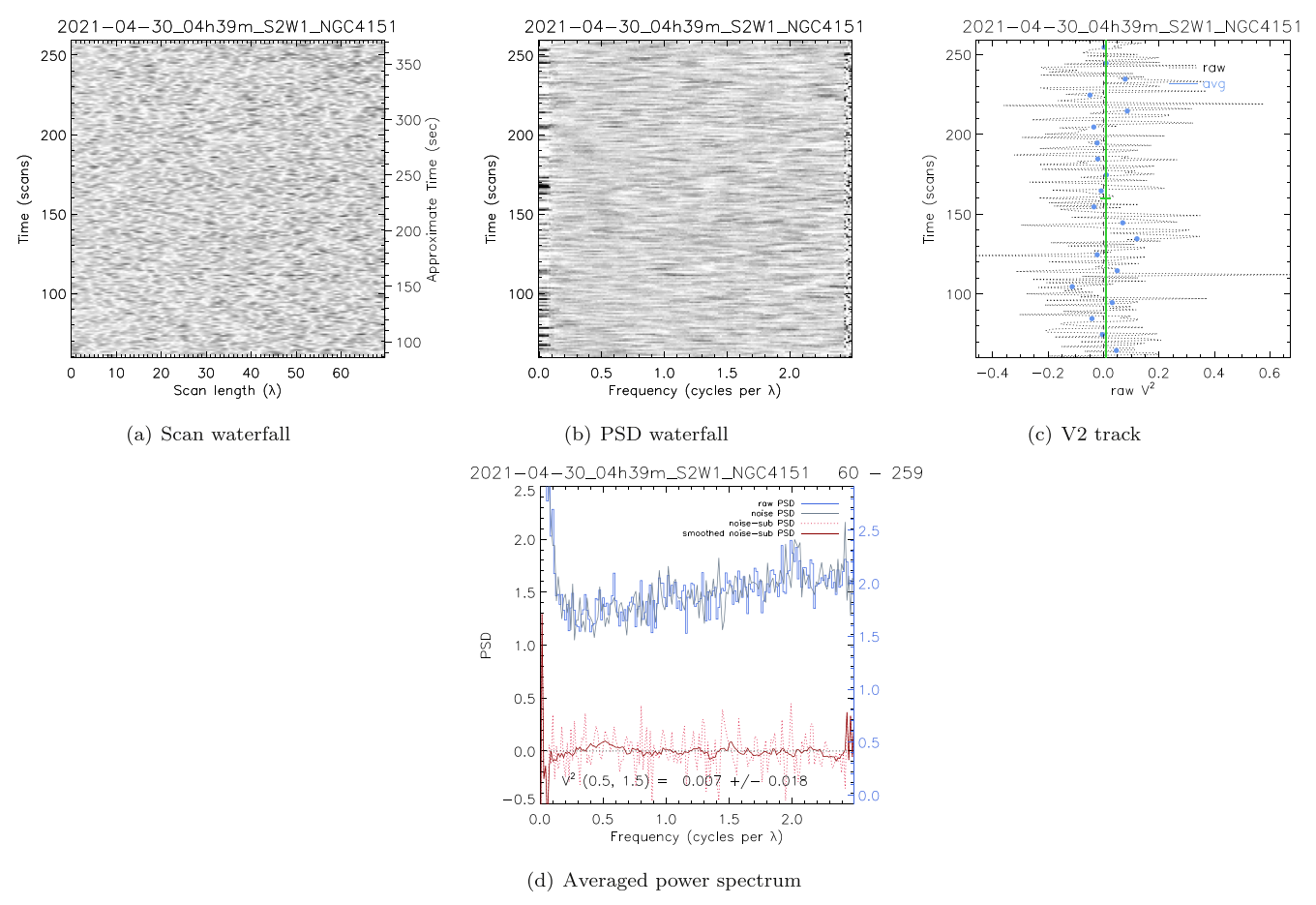


Figure 13. Details of the fringe track #01 for NGC 4151 on 2021 April 30, in the same format as in Figure 7.

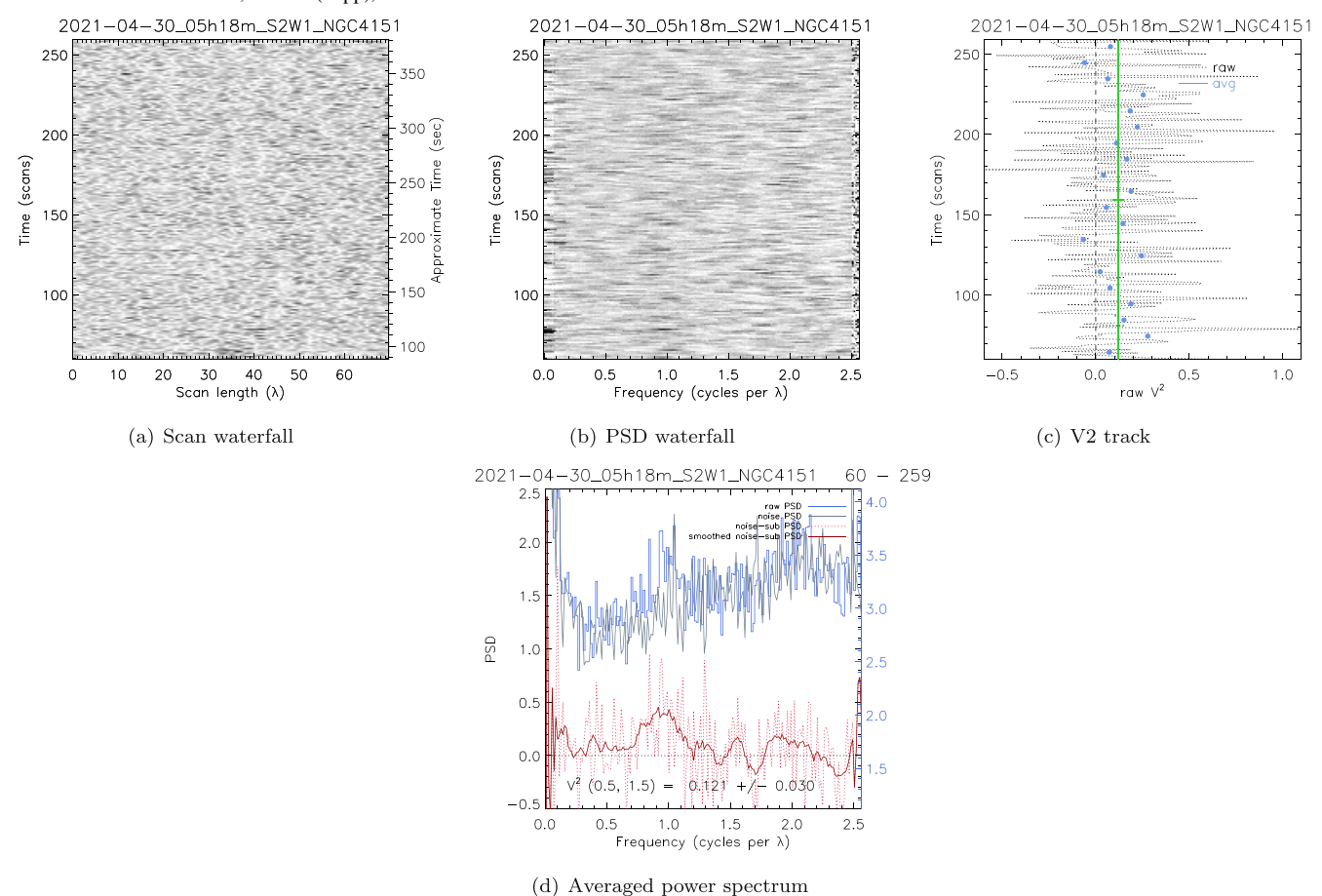
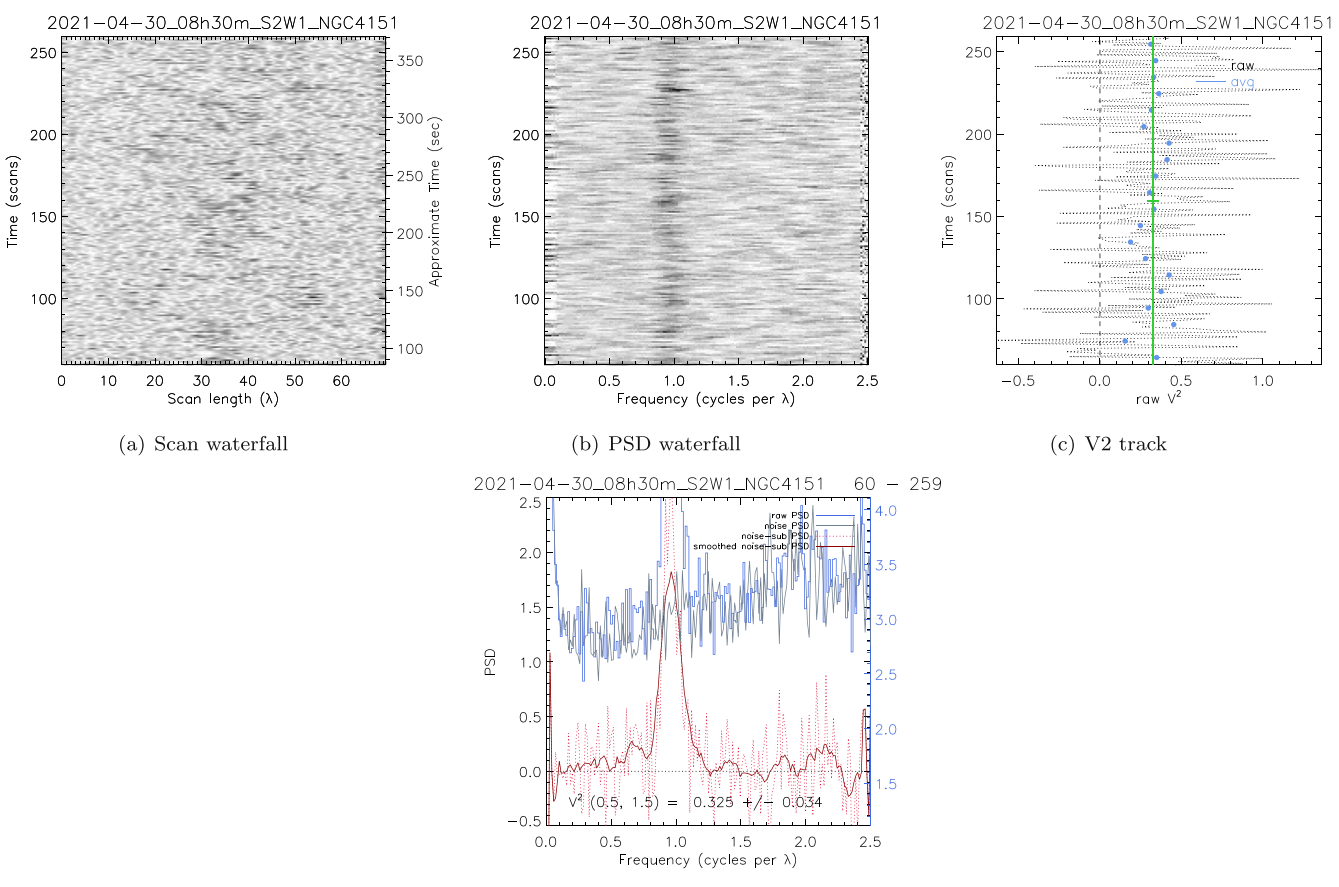


Figure 14. Details of the fringe track #02 for NGC 4151 on 2021 April 30, in the same format as in Figure 7.



(d) Averaged power spectrum

Figure 15. Details of the fringe track #03 for NGC 4151 on 2021 April 30, in the same format as in Figure 7.

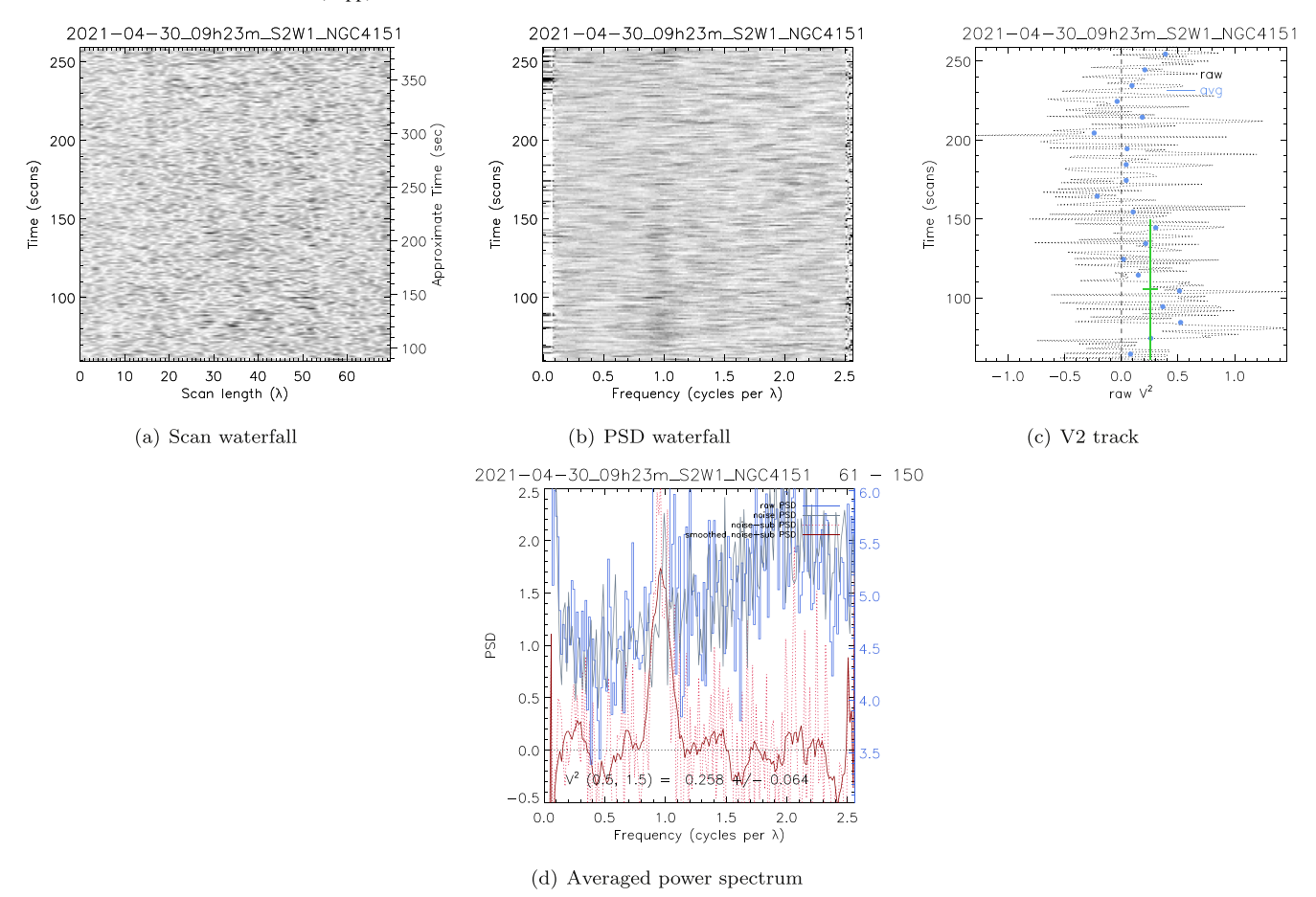


Figure 16. Details of the fringe track #04 for NGC 4151 on 2021 April 30, in the same format as in Figure 7.

ORCID iDs Makoto Kishimoto https://orcid.org/0000-0002-2216-3252

Christopher Farrington https://orcid.org/0000-0001-9939-2830
Sebastian Hönig https://orcid.org/0000-0002-6353-1111
Konrad R. W. Tristram https://orcid.org/0000-0001-8281-5059
Gerd Weigelt https://orcid.org/0000-0001-9754-2233
Gail Schaefer https://orcid.org/0000-0001-5415-9189

References

```
Antonucci, R. R. J. 1983, Natur, 303, 158
Antonucci, R. R. J., & Miller, J. S. 1985, ApJ, 297, 621
Anugu, N., ten Brummelaar, T., Turner, N. H., et al. 2020, Proc. SPIE, 11446,
   1144622
Burtscher, L., Meisenheimer, K., Tristram, K. R. W., et al. 2013, A&A,
   558, A149
Chan, C.-H., & Krolik, J. H. 2016, ApJ, 825, 67
Chan, C.-H., & Krolik, J. H. 2017, ApJ, 843, 58
Che, X., Sturmann, L., Monnier, J. D., et al. 2013, JAI, 2, 1340007
Das, V., Crenshaw, D. M., Hutchings, J. B., et al. 2005, AJ, 130, 945
Dorodnitsyn, A., Kallman, T., & Proga, D. 2016, ApJ, 819, 115
Fernandez, B. R., Holloway, A. J., Meaburn, J., Pedlar, A., & Mundell, C. G.
                 S. 305, 319
Gámez Rosas, V., Isbell, J. W., Jaffe, W., et al. 2022, Natur, 602, 403
GRAVITY Collaboration, Dexter, J., & Shangguan, J. 2020, A&A, 635, A92
Hönig, S. F. 2019, ApJ, 884, 171
Hönig, S. F., & Kishimoto, M. 2017, ApJL, 838, L20
Hönig, S. F., Kishimoto, M., Antonucci, R., et al. 2012, ApJ, 755, 149
Hönig, S. F., Kishimoto, M., Tristram, K. R. W., et al. 2013, ApJ, 771, 87
Isbell, J. W., Meisenheimer, K., Pott, J. U., et al. 2022, A&A, 663, A35
```

```
Kishimoto, M., Hönig, S. F., Antonucci, R., et al. 2011a, A&A, 527, A121
Kishimoto, M., Hönig, S. F., Antonucci, R., et al. 2011b, A&A, 536, A78
Kishimoto, M., Hönig, S. F., Antonucci, R., et al. 2013, ApJL, 775, L36 Kishimoto, M., Hönig, S. F., Beckert, T., & Weigelt, G. 2007, A&A, 476, 713
Koshida, S., Yoshii, Y., Kobayashi, Y., et al. 2009, ApJL, 700, L109
Krolik, J. H. 2007, ApJ, 661, 52
Krolik, J. H., & Begelman, M. C. 1986, ApJL, 308, L55
Krolik, J. H., & Begelman, M. C. 1988, ApJ, 329, 702
Leftley, J. H., Tristram, K. R. W., Hönig, S. F., et al. 2018, ApJ, 862, 17
Leftley, J. H., Tristram, K. R. W., Hönig, S. F., et al. 2021, ApJ, 912, 96
Lira, P., Goosmann, R. W., Kishimoto, M., & Cartier, R. 2020, MNRAS,
   491, 1
López-Gonzaga, N., Burtscher, L., Tristram, K. R. W., Meisenheimer, K., &
   Schartmann, M. 2016, A&A, 591, A47
López-Gonzaga, N., Jaffe, W., Burtscher, L., Tristram, K. R. W., &
   Meisenheimer, K. 2014, A&A, 565, A71
Martel, A. R. 1998, ApJ, 508, 657
Minezaki, T., Yoshii, Y., Kobayashi, Y., et al. 2004, ApJL, 600, L35
Miyauchi, R., & Kishimoto, M. 2020, ApJ, 904, 149
Mor, R., Netzer, H., & Elitzur, M. 2009, ApJ, 705, 298
Mundell, C. G., Pedlar, A., Baum, S. A., et al. 1995, MNRAS, 272, 355
Mundell, C. G., Wrobel, J. M., Pedlar, A., & Gallimore, J. F. 2003, ApJ, 583, 192
Namekata, D., & Umemura, M. 2016, MNRAS, 460, 980
Ozaki, S. 2009, PASJ, 61, 259
Pedlar, A., Kukula, M. J., Longley, D. P. T., et al. 1993, MNRAS, 263, 471
Pott, J.-U., Malkan, M. A., Elitzur, M., et al. 2010, ApJ, 715, 736
Raban, D., Jaffe, W., Röttgering, H., Meisenheimer, K., & Tristram, K. R. W.
  2009, MI
            VRAS. 394, 1325
Schnülle, K., Pott, J. U., Rix, H. W., et al. 2015, A&A, 578, A57
Smith, J. E., Robinson, A., Alexander, D. M., et al. 2004, MNRAS, 350, 140
Swain, M., Vasisht, G., Akeson, R., et al. 2003, ApJL, 596, L163
ten Brummelaar, T. A., McAlister, H. A., Ridgway, S. T., et al. 2005, ApJ,
  628, 453
Ten Brummelaar, T. A., Sturmann, J., Ridgway, S. T., et al. 2013, JAI, 2,
   1340004
```

Kishimoto, M., Hönig, S. F., Antonucci, R., et al. 2009, A&A, 507, L57

ten Brummelaar, T. A., Sturmann, J., Sturmann, L., et al. 2018, Proc. SPIE, 10703, 1070304

Tristram K. R. W. Burtscher, L. Jaffe, W. et al. 2014, A&A, 563, A&2

Tristram, K. R. W., Burtscher, L., Jaffe, W., et al. 2014, A&A, 563, A82 Ulvestad, J. S., Wong, D. S., Taylor, G. B., Gallimore, J. F., & Mundell, C. G. 2005, AJ, 130, 936

Wada, K. 2012, ApJ, 758, 66

```
Wada, K. 2015, ApJ, 812, 82
Wang, J., Fabbiano, G., Risaliti, G., et al. 2010, ApJL, 719, L208
Weigelt, G., Hofmann, K.-H., Kishimoto, M., et al. 2012, A&A, 541, L9
Williamson, D., Hönig, S., & Venanzi, M. 2019, ApJ, 876, 137
Williamson, D., Hönig, S., & Venanzi, M. 2020, ApJ, 897, 26
```